Numerical fluid simulation of an MPD Thruster with Real Geometry *

G. Caldo[†], E.Y. Choueiri[‡], A.J.Kelly[§], and R.G. Jahn[¶]
Electric Propulsion and Plasma Dynamics Laboratory
Princeton University
Princeton, New Jersey 08544, USA

Abstract

A two-fluid, two-dimensional numerical model for axially symmetric arbitrary-geometry MPD thruster flows including anomalous transport has been developed and used to study the flow in a Full-Scale Benchmark Thruster (FSBT) with argon propellant and under realistic conditions. The innovation with respect to past studies[1, 2] is that the thruster geometry is arbitrary and user-defined. The code prepares an appropriate grid for the given geometry and solves the Euler equations through a finite volumes technique developed from the work of Jameson[3]. Simultaneously, the electromagnetic equation is solved through transformation of coordinates with a modified Jacobi technique for nonlinear equations (see ref. [4]). While our previous constant-area code[2] converged for currents as high as 18 kA (6 g/s of argon) the arbitrary geometry code could not converge for currents higher than 10 kA with only classical transport. The inclusion of anomalous resistivity increased that limit to 13.5 kA. This was still below the so-called critical ionization current (16 kA) above which our previous calculations showed the pronounced impact of anomalous transport on both the flow fields and the performance. Consequently, only trends and milder effects of anomalous dissipation could be observed. The ability of the new code to model real geometry effects was confirmed by the excellent agreement between the predicted current contour around the anode lip with that measured experimentally.

*This work is supported by the Air Force Office of Scientific Research under contract AFOSR-91-0162 and the National Aeronautics and Space Administration under contract NASA-954997.

[†]Graduate Student

[‡]Research Associate

[§]Senior Research Staff

[¶]Professor

Nomenclature

$\mathbf{B}$	magnetic field strength
$\mathbf{E}$	electric field
E	energy density per unit volume
J	total interelectrode current
$\mathbf{j}$	current density
σ	electrical conductivity
ψ	electromagnetic stream function
k	Boltzmann's constant, heat transfer coefficient
m	mass
e	elementary charge
μ_o	permeability of free space
ε_o	permittivity of free space
n	number density
ρ	mass density
p	pressure
T	temperature
$\mathbf{v}$	plasma streaming velocity
Ω	electron Hall parameter
ν	collision frequency
r	radial coordinate
z	axial coordinate
t	time
Subscripts	
e	electron
i	ion
n	neutral
h	heavy species
AN	anomalous
eff	effective
t	thermal
d	drift

Introduction

Numerical fluid simulations of MPD thrusters can be instrumental in studying the two major problems of MPD propulsion, namely efficiency and lifetime. Understanding energy dissipation processes inside the thrust chamber would allow to study ways of increasing efficiency; furthermore, understanding the nature and dependence of heat transfer to the device and of current attachment could have a beneficial impact on the design of longer lifetime thruster. A review of previous fluid simulations of the MPD thruster including our work and those of other researchers can be found in[5].

The tow major requirements for a useful fluid code are the inclusion of relevant physics and processes and the ability to handle real geometries. While our past work[1, 2] has attempted to contribute to the better representation of dissipative processes by including some of the effects of anomalous transport (i.e. transport due to plasma microturbulence) the present work adds the capability of studying real geometries.

The older code which was used to compare MPD thruster operation with and without anomalous transport was modified to model an arbitrary thruster shape, which can be chosen by the code's user. For this study, the Princeton Full-Scale Benchmark Thruster (FSBT) operated with argon was chosen to be modeled. This choice was not motivated by the promise of that geometry (although recent thrust measurements at EPPDyL[6] have indicated that efficiencies as high as 75% could possibly be obtained with hydrogen and deuterium) but rather for two other reasons. First, is the wide experimental database amassed at EPPDyL during more than a decade. Second, is our belief that the anode geometry of the FSBT provides a real challenging test for the robustness of the code and its ability to model real geometries.

1 MPD Thruster Model

1.1 Geometry

A cylindrically symmetric geometry similar to that of the FSBT is employed for this study. This geometry represents a substantial improvement over the constant cross-section geometry used in past papers[1, 2]. The grid-generation program can adapt a variable density grid to any thruster geometry, as long as the domain boundary and the relative gridpoint concentration at the boundary are specified.

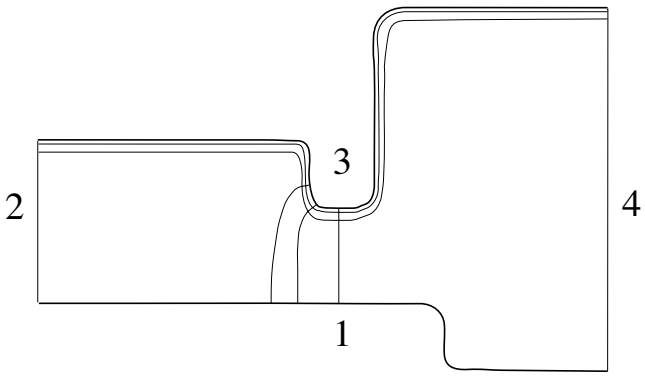

Figure 1: Construction of gridlines.The numbers 1 through 4 indicate the ordering of the input boundary lines.

1.2 The EPPDyL Grid Generator (EGG)

The EGG code is designed to compute quickly smooth curvilinear grids for arbitrary thruster geometries.

Given the geometry specified by the user (see section 1.3), a very fine rectangular grid is superimposed on this geometry as in Fig. 2, and the equation $\nabla^2\eta = 0$ is solved on the points of the grid which correspond to the inside of the thruster. The gridlines that follow boundaries 1 and 3 are then chosen as the lines of constant η on the grid. As for the lines that follow boundaries 2 and 4, lines perpendicular to those of constant η are chosen (see Fig. 1).

The EGG algorithm includes the following steps:

- The code finds a parametric line for each of the four boundaries. This line is simply the collection of segments connecting the points input by the user.
- Superposition of fine rectangular grid on domain (see Fig. 2). The code determines what points belong to the boundary, to the inside and to the solid walls. Once the appropriate flags are hoisted, η will not be computed at points on a solid wall, but will be assigned its value at the closest boundary point.
- Solution of $\nabla^2\eta = 0$ on rectangular grid. An explicit finite difference method is used. The

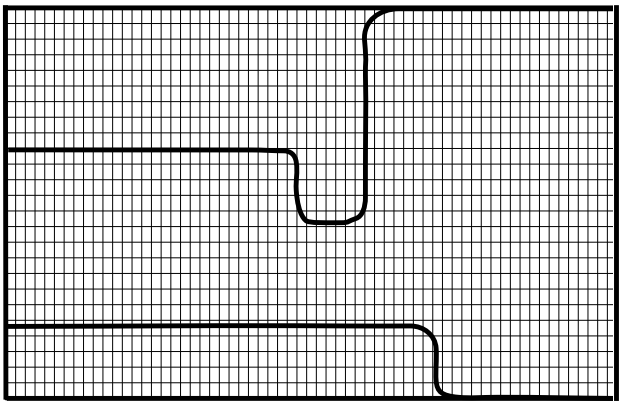

Figure 2: Superimposed rectangular grid.

Boundary conditions are: $\eta = 1$ on boundary 3, $\eta = 0$ on boundary 1, and $\partial\eta/\partial\hat{n} = 0$ on boundaries 2 and 4 (see Fig. 1). This way the lines such that $\eta = 0, \eta = 1$ are exactly boundaries 1 and 3, respectively.

- Construction of lines η_i such that $\eta = \eta_i$ on the lines. For every vertical line of the rectangular grid, a value of r is found so that $\eta(r) = \eta_i$. Because of the great smoothness of the function $\eta(z, r)$, these lines are themselves smooth, no matter how jagged the boundary is (see Fig. 1).

- Determination of gridpoint distribution on boundary 3 using weight functions. The distribution of points on the upper boundary line is found in such a way that the distance between two adjacent nodes is inversely proportional to the weight of the closest boundary point (this is the weight input by the user).

- Construction of lines parallel to boundaries 2 and 4 through the perpendicularity criterion. For each point on boundary 3 computed in the previous step, a line is generated which is perpendicular to all the lines of constant η (see Fig. 1).

- Averaging of the resultant point distribution on the bottom boundary with the distribution input by the user. The perpendicular lines constructed in the previous step end on the bottom boundary with a given distribution. This distribution and the one determined with the method of weights (as in the sixth step) are averaged together and define a final distribution of points on boundary line 1.

- Construction of a final set of lines perpendicular to lines of constant η. These are constructed in the same way as the lines departing from the top boundary, except that they start at the bottom boundary and extend to the top boundary. The intersection between these lines and the lines of constant η is the resultant grid. The grid in Fig. 3 is one example of this kind of grid. It took four hour to compute on a MacIntosh Quadra 700 workstation.

1.3 Graphical Interface

A versatile user-friendly graphical interface was developed by Choueiri[7] to allow a user, who has little or know knowledge of the code's inner workings, to specify the geometry and conditions for the simulation. The front-end of the interface is a panel of Aldus Freehand, a commonly used graphics application for the Macintosh. The user draws the geometry employing the tools of Aldus Freehand and follows simple conventions to prescribe the type of each of the boundaries. There are four choices for boundary types: cathode, anode, insulator and free boundary. The user also has the ability of easily specifying the relative gridpoint density on any location along the boundaries, thus allowing a measure of control over the tailoring of the grid over critical areas in the flow. The interface program, thereafter, decodes the resulting postcript file and extracts all the conditions required as input for the grid generation subroutine and the simulation code.

The resulting computational grid for the present simulation of the FSBT is shown in Fig. (3). The model's dimensions are those of the real thruster, except for a slightly thicker cathode and a shorter, wider anode, adopted to reduce overall grid refinement and thus computational time. The FSBT grid includes the vertical anode and the free surface at the thruster exhaust which was made to extend about two thruster radii downstream of the cathode tip to allow for a good representation of the near-thruster plume.

1.4 Models and Assumptions

The nucleus of the code has been described along in more detail in our previous paper[2]. We refer the interested reader there for a description of the equations and the adopted numerical methods. Only

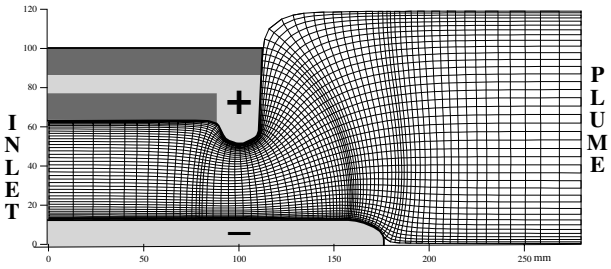

Figure 3: Benchmark Thruster geometry and curvilinear grid used for computation.

a summary of these and a description of the new issues are given below.

The code represents a two-fluid, axisymmetric, two-dimensional model with separate conservation for the electron and heavy species energies. Viscous effects are not treated at this stage since the code has been used primarily to study the effects of anomalous dissipation which could be hard to untangle from viscous dissipation. Electron-electron and ion-ion heat conduction is included. It is also assumed that the electrons obey the ideal gas law, while the ions obey a non-ideal equation of state. The numerical derivation of this equation from accurate argon partition functions is discussed in ref. [8]. The polynomial fit to the function is contained in ref. [5]. A Hall term has been introduced in Ohm's law, and no applied magnetic field is assumed. The net electron production rate $\dot{n}_e$ is calculated using the Hinnov-Hirshberg theory of ionization-recombination[9]. The effective conductivity σ_{eff} is computed using Choueiri's anomalous transport models[10] cast in polynomial using a two-parameter, variable cross-term, least square fit[1]. The heat transfer coefficient is that derived in Mitchner and Kruger[9]. The energy density per unit volume E_h is defined as

$$E_h = \frac{p_h}{\gamma - 1} + \frac{\rho}{2}(v_z^2 + v_r^2)$$

and similar definition applies for E_e.

The flow field code uses a finite volumes discretization with artificial dissipation described by Jameson[11]. The time stepping is done via the third order multistage scheme described in ref. [12], and convergence is accelerated using a multigrid iteration first proposed by Jameson and Jayram[13]. These methods yield a second order steady-state solution to the conservation equations. The solution of the conservation equations through the finite volumes/Euler forward routine is alternated with the solution of the electromagnetic equation, until consistency among all the parameters is achieved.

The stream function equation is solved with a second-order nonlinear explicit scheme developed at EPPDyL (modified Jacobi routine).

The model was coded in APL2 (taking full advantage of the inherent vectorizing capability of the language) and has been run on a variety of machines ranging from a MacIntosh Quadra 950 (1.2 Mflops) to an IBM ES/3090 600J Supercomputer, where specialized APL2 compilers can allow convergence to be reached in a few tens of minutes.

1.5 Boundary Conditions

Compared to a rectangular geometry code like the one presented in refs. [1, 2], a curvilinear grid code requires different boundary conditions for different surfaces. A list of the boundary conditions on each line or surface follows:

- *Inlet.* The heavy species temperature is fixed to 10^4 K, the mass flow rate to either 6 or $16 g/s$, and the Mach number to 1. The electron temperature is taken to satisfy $\partial T_e/\partial z = 0$ at $z = 0$. The radial velocity is set to 0. The value of the total current J specifies the stream function value: $\psi = 4\pi J/\mu_0$. The fluid velocity is determined from the Mach number and the heavy species temperature. The inlet density is taken to be uniform and such that $2\pi \int_r \rho v_z r dr = \dot{m}$. The ionization ratio is taken so as to make $\dot{n}_e = 0$, i.e., there is no net electron production at the inlet.

- *Electrodes.* Here the parallel electrode field must be zero, and this implies solving the boundary equation $E_z = 0$ concurrently with the ψ equation[14].

- *Insulators.* The stream function is here constant and proportional to the amount of current flowing downstream of the insulators.

- *Solid boundaries.* Heavy species temperature is here fixed, while electron temperature has zero normal derivative. The perpendicular component of the velocity is set to zero, where the parallel component has zero normal derivative. Electron and heavy species densities are set to have zero normal derivatives.

- *Thruster axis.* Here all flow parameters have zero radial derivatives, by symmetry. In addition, radial velocity is zero.

- *Free boundaries.* The normal second derivative is set to zero, so as to make the normal derivative vary linearly between the inside and the boundary. The normal derivative of the stream function is set to zero.

2 Results

Runs were made both with and without anomalous transport dissipation terms present in the calculation. While our previous constant-area code[2] converged for currents as high as 18 kA (6 g/s of argon) the present arbitrary-geometry code could not converge for currents higher than 10 kA with only classical transport. The inclusion of anomalous resistivity increased that limit to 13.5 kA.

It is important to report that divergence always occurred through strong oscillations of the electron energy density in the time-stepping routine with the electron temperature going negative or increasing exponentially. The strongly nonlinear term in the E_e equation is j^2/σ_{eff}, which is proportional to $E_e^{\frac{3}{2}}$, and grows as the square of the total current. As J increases, the time-stepping interval for convergence quickly tends to zero.

The highest current at which this code converges is quite lower than that of a constant cross-section geometry (about 18kA, from ref. [2]). This is because a curvilinear grid, however smooth, introduces substantial multipliers to the equations' gradients, leading to a reduced convergence spectrum. The reason why classical runs diverge at lower J's than anomalous runs is not clear, but this also might be related to the curvilinear geometry, since exactly the *opposite* effect was observed for the constant cross-section case.

The fact that the cause of the divergence always lies in the electron energy equation and the fact that the electron temperature increases asymptotically to unrealistic levels when divergence occurs, are also indicative of the lack of proper representation of energy sinks in the electron energy. Proper represntation of electron energetics is clearly one of the major improvements still needed for such fluid codes. It is important to state in this context that the inclusion of finite equilibration rates in many processes and the inclusion of microturbulent effects on ionization[15] should render the electron energy equation more realistic and thus better behaved.

2.1 Anomalous Transport Scaling

The highest level reached by the classical code[1] was 10 kA while that for the anomalous runs was 13.5 kA. This was still below the so-called critical ionization current (16 kA) above which our previous calculations showed the pronounced impact of anomalous transport on both the flow fields and the performance. Consequently, unlike in ref. [2] where we investigated in detail the effects of anomalous transport, only trends and milder effects of anomalous dissipation could be observed here.

As previously discussed in refs. [5] and [16], anomalous resistivity is conditionned to occur in regions of the discharge where the ratio of the electron drift velocity to te the ion thermal velcity, u_{de}/v_{ti}, exeeceds about 1.5. Therefore the parameter u_{de}/v_{ti} plays the role of a switch for microturbulent (or anomalous) dissipation. In regions where $u_{de}/v_{ti} \geq 1.5$ anomalous effects generally become a strongly increasing function of the electron Hall parameter Ω_e and a weakly increasing function of T_i/T_e.

The data shown in Figs. 9,10,11,and 12 were chosen from for the anomalous run with $J = 10KA$, $\dot{m} = 6g/s$ because that was the highest current level at which both anomalous and classical runs converged.

Fig. 9 presents a contour plot of u_{de}/v_{ti}. The regions where anomalous transport is active $u_{de}/v_{ti} \geq 1.5$ lie close to the tip of the cathode and around the entire anode. As the current grows, the electron drift velocity increases, while the thermal velocity of the ions increases much more slowly. This means that for higher currents than $10KA$ the anomalous transport activation area should become larger. This is indeed confirmed by the 13.5 kA anomalous runs and our earlier simulations[2].

Fig. 10 shows the Hall parameter distribution over the FSBT. Regions of enhanced Hall parameter around the anode region can already be seen at this low current. The upstream region of the near-cathode plasma, especially the root, is a location where anomalous effects are of importance as already discussed in [2].

Fig. 11 shows the map for T_i/T_e which is another,

[1] The runs in which the conservation equations include anomalous transport coefficients are refered to as "anomalous", whereas those not containing anomalous transport are called "classical runs".

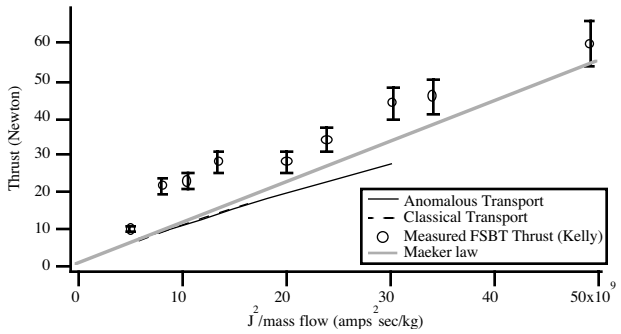

Figure 4: Calculated thrust from simulations with and without anomalous transport compared with FSBT thrust measured by Miller and Kelly [17].

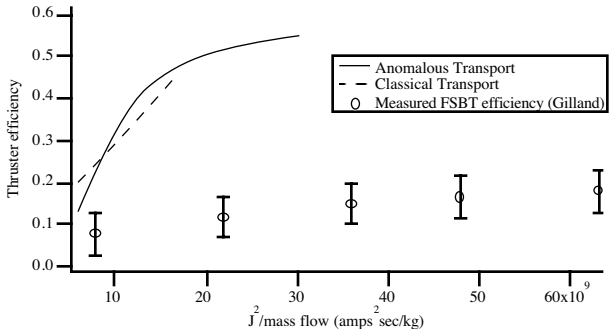

Figure 5: Thrust efficiency for simulations with and without anomalous transport compared with measured FSBT values (Gilland). Theory, unlike experiments, does not include electrode sheath drops

albeit weak, scaling parameter for anomalous resistivity.

The maps in Figs. 9,10,11 together give a picture of the regions where anomalous resistivity becomes important. This picture is distilled in Fig. 12 which shows a field plot of the ratio between resistivities obtained for an anomalous run and for a classical run, again with $J = 10KA$, $\dot{m} = 6g/s$. Again, even at this relatively low current evidence of anomalous resitivity can be seen around the anode lip. More strikingly, the plasma region adjacent to the cathode near the thruster's exit plane and that at the cathode root show the most evidence of anomalous resitivity.

2.2 Performance Curves

As is evident from Fig. (4), thrust scales linearly as the square of the current individually for the case with and without anomalous transport.

At low values of $J^2/\dot{m}$, classical and anomalous thrust overlap, and are both close than the Maeker law curve. For $J^2/\dot{m}$ exceeding 15 kA $2/sg$, the numerical model underpredicts thrust somewhat because the artificial viscosity introduced to assure code convergence has, on the average, the effect of slowing down the fluid in the nozzle.

Efficiency is calculated through integrating the energy flux $1/2\rho(v_z^2 + v_r^2)\mathbf{v}$ over the domain's free surface, dividing by the total thrust power and subtracting the result from one. In Fig. (5) the efficiency is plotted, again, versus $J^2/\dot{m}$. It is important to note here that the experimental data shown in this figure naturally take into account the effects of the electrode sheath drops which are not modelled in the code. If the experimental total voltage were reduced by the sheath voltage, the numerical and experimental curves would approach each other significantly. Gallimore[18], in fact, has shown that the anode fall voltage increases monotonically with $J^2/\dot{m}$, and reaches values as high as 40 volts around $J^2/\dot{m} = 50\text{kA}^2$ sec/g.

The classical code diverged at a current too low to allow drawing a conclusion on the difference between the two types of simulations. We know however, from our previous simulation that, at high currents, a code with anomalous transport predicts efficiencies as much as 15 % lower than those predicted by a code with only classical transport. A trend of levelling off at high currents ($J^2/\dot{m} > 30KA^2\ sec/g$) can be seen in the "anomalous" curve which hints at such a behavior.

2.3 Parameter Distribution Over Real Thruster Geometry

In this section, space plots of relevant parameters will be discussed in relation to their behavior over a complex geometry.

Fig. 7 shows that current is clearly blown downstream. The outer anode-insulator interface is subject to significant attachment, while at this low current level (10kA, 6 g/s) no severe cathode root attachment is noticed. Gas velocity, plotted in Fig. 6, increases significantly downstream of the anode lip; this is a clear effect of supersonic expansion of the gas. At this current level, in fact, the pressure gradient force is of the same order as the electromagnetic

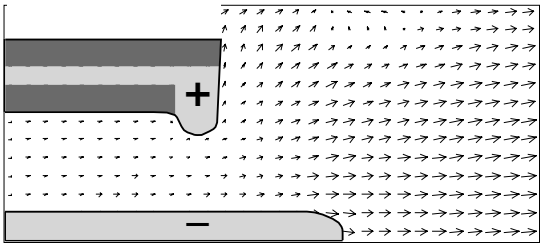

Figure 6: Gas velocity distribution; $J = 10KA$, $\dot{m} = 6g/s$.

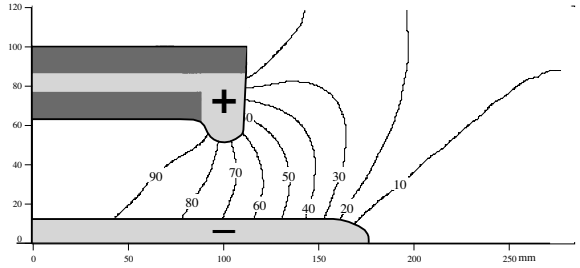

Figure 7: Current contour lines; $J = 10KA$, $\dot{m} = 6g/s$.

force. The reduction of the flow velocity in the area downstream above the anode may be due to the $-z$ orientation of the magnetic force next to the insulator.

Fig 13 shows that heavy species pressure is greatest immediately upstream of the anode lip, where the dynamic pressure largely transforms into static pressure. At the tip of the cathode, furthermore, p_h is also large because the pumping force is directed in the $-\hat{r}$-direction. The pressure distribution is thus qualitatively realistic.

One test for the code's ability to model the peculiarity of a real geometry such as that of the FSBT is to compare the simulations to measurements around the anode lip.

Fig. 8 shows current contour lines around the anode for classical and anomalous simulations as compared to Gallimore's experimental findings at $16KA$, $16g/s$. At this low value of $J^2/\dot{m}$, small, if any differences can be seen between the classical and anomalous runs. Agreement between the measured and predicted current distributions is excellent within the experimental error bar.

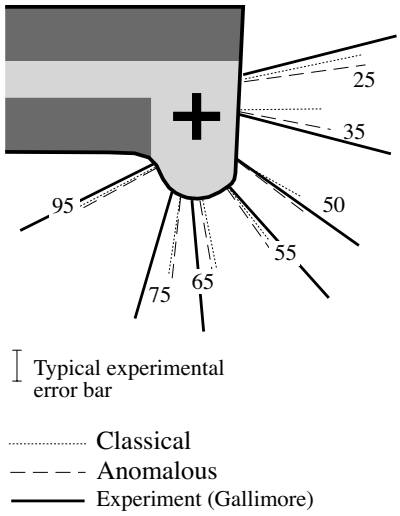

Figure 8: Enclosed current lines on an MPD thruster anode, $16KA$, $16g/s$. The numbers represent the percentage of total current downstream of the line.

Conclusions and Final Remarks

A two-fluid, two-dimensional numerical model for axially symmetric arbitrary-geometry MPD thruster flows including anomalous transport has been developed and used to study the flow in a Full-Scale Benchmark Thruster (FSBT) with argon propellant and under realsitic conditions.

The code could not converge for currents higher than 10 kA with only classical transport. The inclusion of anomalous resistivity increased that limit to 13.5 kA. This was still below the so-called critical ionization current (16 kA) above which our previous calculations showed the pronounced impact of anomalous transport on both the flow fields and the performance. Flow field maps and performance curves were obtained using the code and discussed in relation to the FSBT geometry.

The ability of the new code to model real geomtery effects was confirmed by the excellent agreement between the predicted current contour around the anode lip with that measued experimentally.

There are still improvements that can be applied to the model presented above. The numerical solution to the fluid equations could still benefit from techniques and changes that would make it even more robust and guarantees convergence for simulations at medium-high current levels. Furthermore, both converegence and realism could be better at-

tained if the physics of the model include an accurate representation of viscosity, of non-equilibrium rate kinetics and a more realistic ionization model including microturbulent effects.

References

[1] G. Caldo, E.Y. Choueiri, A. J. Kelly, and R. G. Jahn. An MPD code with anomalous transport. In 22^{nd} *International Electric Propulsion Conference*, Viareggio, Italy, 1991. IEPC-91-101.

[2] G. Caldo, E.Y. Choueiri, A.J. Kelly, and R.G. Jahn. Numerical simulation of MPD thruster flows with anomalous transport. In 28^{th} *Joint Propulsion Conference*, Nashville, Tennessee, 1992.

[3] A. Jameson. Transonic flow calculations. Technical Report MAE 1651, Princeton University, 1983.

[4] H. Jacoby. Entwicklung eines teoretischen modells zur beschreibung der wechselwirkung zwischen elektrischer entladung und uberschallstromung eines gepulsten co-lasers. Master's thesis, Institut fur Technische Physik, Stuttgart, 1984.

[5] G. Caldo. Numerical simulation of MPD thrusters with anomalous transport. Master's thesis, Princeton University, 1994.

[6] J. Kline and C. Niederstrasser. MPD thruster performance measurement with hydorgen and deuterium. Contribution to the May/Jugust 1993 Bimonthly Progress Report of the Electric Propulsion and Plasma Dynamics Laboratory. Technical Report MAE 1776.43, EPPDyL, Princeton University, 1993.

[7] E.Y. Choueiri. A user-friendly graphical interface for MPD thruster fluid simulation codes. Contribution to the July/August 1993 Bimonthly Progress Report of the Electric Propulsion and Plasma Dynamics Laboratory. Technical Report MAE 1776.44, EPPDyL, Princeton University, 1993.

[8] E.Y. Choueiri. A scaling strategy for the preliminary design of MPD thrusters. Master's thesis, Syracuse University, Syracuse, New York, 1983.

[9] M. Mitchner and C.H. Kruger. *Partially ionized Gases*. Wiley Interscience, New York, 1973.

[10] E.Y. Choueiri, A.J. Kelly, and R.G. Jahn. Curent-driven plasma acceleration verus current-driven energy dissipation. Part III: Anomalous transport. In 28^{th} *Joint Propulsion Conference*, Nashville, Tennessee, 1992.

[11] A. Jameson. Steady-state solution of the euler equations for transonic flow. Technical Report MAE 1643, Princeton University, 1983.

[12] A. Jameson. Numerical solution of the euler equation for compressible inviscid fluids. Technical Report MAE 1643, Princeton University, 1983.

[13] M. Jayaram and A. Jameson. Multigrid solutions for the Navier-Stokes solutions for flow over wings. In 26^{th} *Aerospace Science Meeting*, Reno, Nevada, 1988. AIAA-88-0705.

[14] P.C. Sleziona, M. Awter-Kurtz, and H. O. Shrade. Numerical evaluation of MPD thrusters. In 21^{st} *International Electric Propulsion Conference*, Orlando, Florida, 1990. AIAA-90-2602.

[15] E.Y. Choueiri and H. Okuda. Anomalous ionization in the MPD thruster. In 23^{nd} *International Electric Propulsion Conference*, Seattle, Washington, 1993. IEPC 93-067.

[16] E.Y. Choueiri. Anomalous transport models for numerical simulation of MPD thruster plasma flows. Contribution to the January-February Bimonthly Progress Report of the Electric Propulsion and Plasma Dynamics Laboratory. Technical Report MAE 1776.35, Electric Propulsion and Plasma Dynamics Laboratory, Princeton University, 1992.

[17] G.E. Miller and A.J. Kelly. Plasma thrusters performance studies. Contribution to the July/August Bimonthly Progress Report of the Electric Propulsion and Plasma Dynamics Laboratory. Technical Report MAE 1776.38, Electric Propulsion and Plasma Dynamics Laboratory, Princeton University, 1992.

[18] A.D. Gallimore, A. J. Kelly, and R. G. Jahn. Anode power deposition in MPD thrusters. In 22^{nd} *International Electric Propulsion Conference*, Viareggio, Italy, 1991. IEPC-91-125.

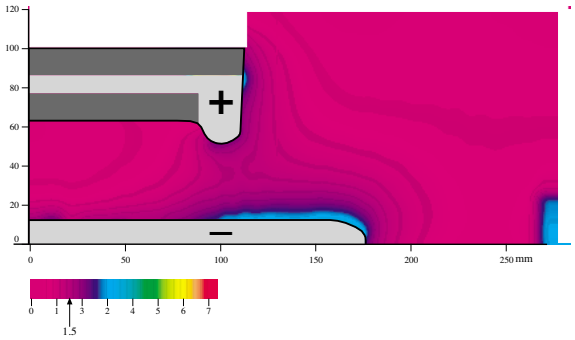

Figure 9: u_{de}/v_{ti} distribution for a run with anomalous transport, $J = 10KA$, $\dot{m} = 6g/s$.

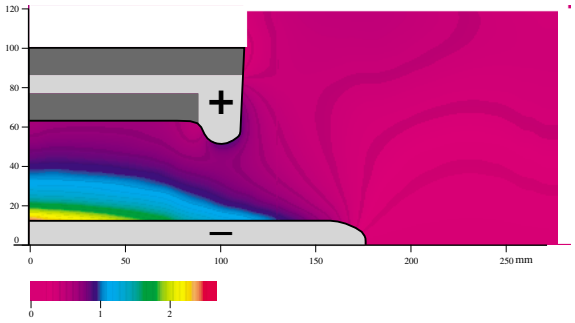

Figure 10: Electron Hall parameter distribution for a run with anomalous transport, $J = 10KA$, $\dot{m} = 6g/s$.

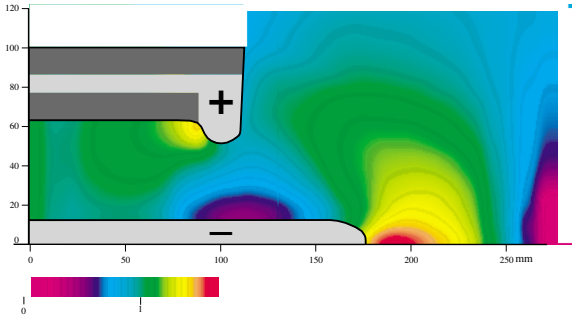

Figure 11: T_i/T_e distribution for a run with anomalous transport, $J = 10KA$, $\dot{m} = 6g/s$.

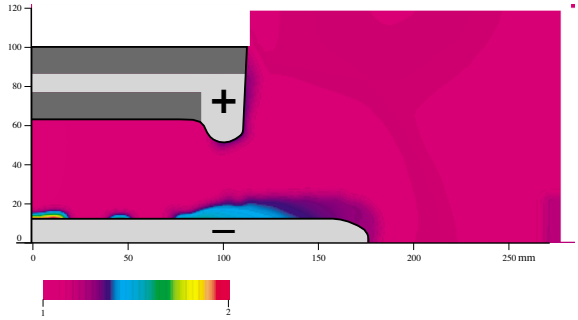

Figure 12: Ratio of resistivities for an anomalous and a classical run, respectively; $J = 10KA$, $\dot{m} = 6g/s$.

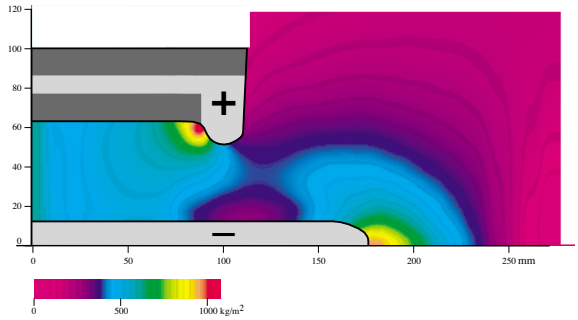

Figure 13: Heavy species pressure distribution; $J = 10KA$, $\dot{m} = 6g/s$.